IEEE Transactions on Quantum Engineering

Received 24 March 2025; revised 24 September 2025; accepted 24 December 2025; date of publication 12 January 2026; date of current version 29 January 2026.

Digital Object Identifier 10.1109/TQE.2026.3653126

Bridging All-Photonic and Memory-Based Quantum Repeaters

NAPHAN BENCHASATTABUSE[1] (Member, IEEE), MICHAL HAJDUŠEK[1], AND RODNEY VAN METER[2] (Senior Member, IEEE)

[1]Graduate School of Media and Governance, Keio University, Fujisawa 252-0882, Japan
[2]Faculty of Environment and Information Studies, Keio University, Fujisawa 252-0882, Japan

Corresponding author: Naphan Benchasattabuse (e-mail: whit3z@sfc.wide.ad.jp).

An earlier version of this paper was presented in part at the 2024 IEEE International Conference on Quantum Computing and Engineering (QCE) [DOI: 10.1109/QCE60285.2024.00217].

This work was supported by the Japan Science and Technology Agency through the Moonshot R&D Program under Grant JPMJMS226C.

ABSTRACT The all-photonic quantum repeater scheme based on repeater graph states (RGSs) offers a promising approach for constructing quantum networks without relying on long-coherence-time quantum memories, which remain a significant technological challenge. Despite substantial progress in defining new schemes for generating RGSs, and in analyzing their performance for the task of secret key generation, the integration of all-photonic schemes with memory-equipped quantum repeaters remains underexplored. We propose an architecture that enables seamless interoperability between all-photonic and memory-based quantum repeaters through an emitter–photon qubit building block, significantly reducing the number of quantum memories required at end nodes from a multiplicative dependence on the trial rate and the number of RGS arms to an additive scaling. The core idea of our architecture is to abstract the all-photonic sections of the network as link-level connections between memory-equipped nodes, enabling integration into existing network-level protocols. In addition, we outline the content and semantics of the messages necessary for a communication protocol based on graph state manipulation rules for computing Pauli frame corrections for obtaining the correct Bell pair. Our approach also provides a simplified method for calculating state fidelity directly from graph state properties.

INDEX TERMS All-photonic repeaters, graph states, network protocols, quantum communication, quantum networking, quantum repeaters.

I. INTRODUCTION

Quantum repeaters [2], [3] are crucial for the realization of quantum networks and the Quantum Internet [4], [5], [6], [7], which have the potential to transform secure communication [8], [9], [10], private delegated quantum computation [11], [12], distributed quantum computing [13], [14], [15], sensing [16], [17], [18], and metrology [19], [20], [21], [22], among other quantum communication applications. Repeaters are placed along the communication path to segment it into shorter links, increasing the success probability of entanglement distribution in the presence of optical fiber attenuation. These short-length entanglements splice into long-distance entanglement shared between distant users [23], [24].

Among various quantum repeater proposals, all-photonic quantum repeaters based on repeater graph states (RGSs) [25] stand out by eliminating the need for long-lived quantum memories, which pose significant technical challenges, decoupling quantum memory development from the realization of quantum repeaters. Highly entangled photonic states are used instead of stationary quantum memories to increase the redundancy, allowing them to be corrected and turned into the desired states as long as a certain subset of the photons is not lost during the transmission. In addition, these repeaters also offer fast entanglement distribution rates limited only by the speed of the photonic state creation and tolerance of both operational errors and losses, making them fall under the third generation of quantum repeaters [26].

While there is progress in understanding secret key generation rates [27], [28] and improving highly entangled photonic state generation theoretically [29], [30], [31], [32] and experimentally [33], [34], [35], [36], [37] for all-photonic quantum repeaters, it is unclear how memory-equipped end

nodes best participate for applications beyond quantum key distribution (QKD). For QKD applications, end nodes can measure their qubits without the need to wait for swapping success or operations to be applied to obtain the intended states since they can be classically postprocessed. On the other hand, applications beyond QKD, such as distributed quantum computation [38], [39], [40], require Bell pairs to be in a known specific state to operate properly. This requirement creates an operational disparity: all-photonic repeater chains generate entanglement at a high trial rate, while end nodes must hold their participating qubits in quantum memories as they await heralded success messages. To keep pace with this rate, a memory-equipped node must therefore possess a significant number of memories just to buffer states. Other examples of understudied engineering challenges are the integration of all-photonic quantum repeaters with conventional memory-based quantum repeaters for internetworking, explicit communication protocols deciding the actions of how each node participates in the distribution of Bell pairs along the connection path, or resource management policies to allow continuous operation of networks of all-photonic quantum repeaters under complex traffic [41].

Here, we build upon the all-photonic scheme proposed by Azuma et al. [25] and propose a new quantum repeater architecture and communication protocols that address the compatibility issues between all-photonic and memory-based repeaters. Our first contribution is the introduction of the *half-RGS*, an emitter–photon building block that bridges the two architectures by providing a resource-efficient method for any memory-equipped node—whether an end node or a conventional memory-based repeater—to terminate an all-photonic connection. This interface significantly reduces resource demands at end nodes, particularly by minimizing the number of required emissive memories (memory qubits capable of emitting entangled photons) from multiplicative dependence on trial rate and RGS arms to additive scaling. It also enables the implementation of applications reliant on quantum memories compared to previous work [28].

Our second contribution is the abstraction of all-photonic sections as link-level connections, allowing them to integrate seamlessly into existing network-level protocols designed for memory-based repeaters. These protocols, extensively studied for scheduling, fidelity, and purification, can now be applied uniformly across hybrid networks. This abstraction simplifies the architecture while enhancing flexibility and scalability.

Finally, we provide detailed communication protocols for Pauli frame corrections, specifying how photons are measured and how information is processed and transmitted between nodes. Our approach also offers a graphical method based on graph state manipulation rules for calculating the fidelity of distributed Bell pairs without relying on the stabilizer formalism.

The rest of this article is organized as follows. In Section II, we provide the necessary preliminaries on graph states, including their definitions and their extended definition, manipulation rules, and the effects of measurements on their structure. Section III offers an overview of the all-photonic quantum repeater based on the RGS, highlighting its operational principles and its engineering challenges. Section IV introduces our core contribution, the "half-RGS," an emitter–photon interface building block designed to bridge all-photonic and memory-based quantum repeaters while reducing resource demands at end nodes. In Section V, we describe the generation process of the half-RGS building block, building upon the work in [27] and [29]. Section VI presents a full communication protocol, including explicit Pauli frame calculations, first in a generation-agnostic manner and then within our proposed framework using the half-RGS interface. In Section VII, we leverage this framework to derive the fidelity of the distributed Bell pairs, offering a simplified reasoning approach based on graph state properties. Finally, Section VIII concludes this article with a discussion on the implications of our results, potential extensions, and open challenges in heterogeneous quantum network architectures.

II. PRELIMINARIES: GRAPH STATES

The workings of the RGS scheme are best explained with the graph state formalism [42]. The graph state formalism is the main tool in this article that we will use to explain and reason about our architecture, protocols, and also about Pauli frame corrections and fidelity estimation. Here, we provide a brief description of graph states and the required manipulation rules. For a more detailed reading of graph states and their application, we refer readers to [43], [44], and [45].

A. GRAPH STATE DEFINITION

Graph states [42] are a class of quantum states that can be represented via a simple graph $G(V, E)$, where V is the set of vertices and E is the set of edges connecting vertices in V. In the graph state formalism, a vertex represents a qubit initialized in $|+\rangle$ while an edge represents an interaction between two qubits given by the controlled-phase gate $CZ = |0\rangle\langle 0| \otimes I + |1\rangle\langle 1| \otimes Z$. Thus, a graph state defined from $G(V, E)$ can be described as

$$|G(V,E)\rangle = \prod_{\{u,v\}\in E} CZ(u,v)\,|+\rangle^{\otimes |V|}. \tag{1}$$

Graph states defined by (1) are a subclass of more general stabilizer states [46]. They can be described in terms of stabilizer generators

$$g_u = X_u \bigotimes_{v\in N_u} Z_v \tag{2}$$

associated with each vertex u in V, where N_u is the set of neighbor vertices of u.

Stabilizer states are equivalent to some graph states up to local Clifford operators [47], [48], [49]. In other words, for any stabilizer state $|\psi\rangle$, there is a (possibly nonunique) graph

IEEE Transactions on Quantum Engineering

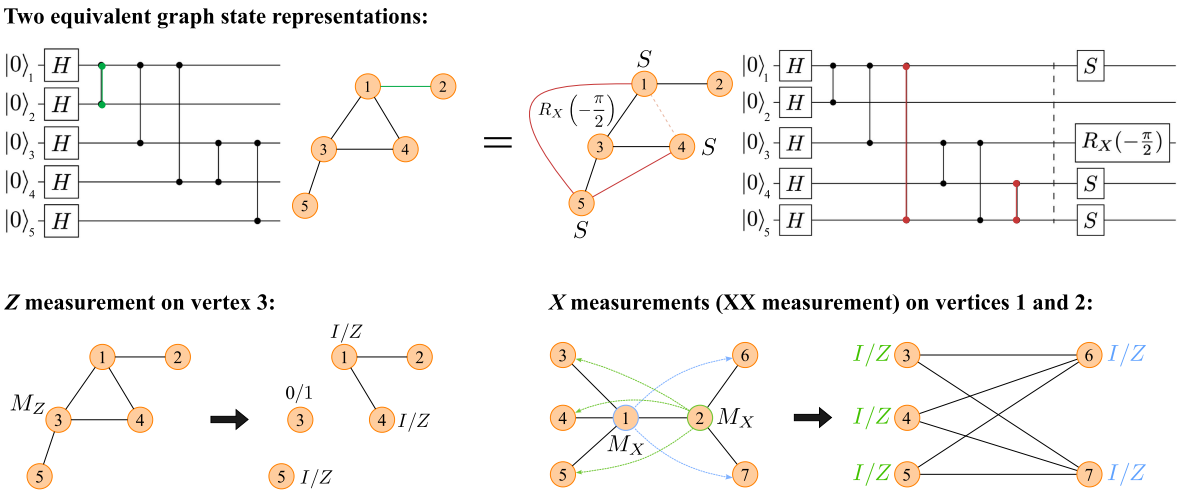

FIGURE 1. Two graph state representations of the same quantum state are depicted at the top. Here, vertices represent qubits in the quantum circuit, and the application of a controlled-phase gate between two qubits corresponds to an edge between the corresponding vertices. An example of such an edge is highlighted in green in the top left. The graph state on the top right is obtained by altering the description through local complementation on vertex 3. This process deletes any existing edges between neighboring vertices of vertex 3, such as the edge (1,4) in this case, and introduces new edges that were previously absent, highlighted in red as (1,5) and (4,5). The application of the depicted Clifford operations ensures that despite the differing graph representations, the quantum states remain identical in both cases. Visualization of a Z measurement with side effects is presented in the bottom left, while the impact of two X measurements (XX measurement) on a different graph is illustrated in the lower right. The Clifford side effects (I/Z) of qubits 3, 4, and 5 depend on the measurement outcome of qubit 2, while those of qubits 6 and 7 hinge on the outcome of qubit 1, as indicated by the blue and green arrows.

state description $|G, \underline{C}\rangle$

$$|\psi\rangle = |G; \underline{C}\rangle = |G; C_1, C_2, \ldots, C_n\rangle = \bigotimes_{i=1}^{n} C_i\,|G\rangle \qquad (3)$$

where $C_i \in \mathcal{C}_1$ is a single-qubit Clifford gate acting on qubit i, with $\mathcal{C}_1$ being the local Clifford group (single-qubit Clifford gates). We call the Clifford operator acting on each vertex of the graph "Clifford side effect" or just "side effect" when the context is clear. These side effects when drawn are represented by a letter next to the vertex, as shown in Fig. 1. We will use this definition of graph states with Clifford side effects as tools for reasoning and understanding the RGS scheme and our protocol.

Typically, (1) is used when we only care about the entangled properties of the states without tracking the actual states as long as they are local Clifford equivalent. Here, we emphasize that we must track the side effects as in (3) because we need to be able to know the exact quantum states shared between end-to-end to get Bell pairs in the correct state.

B. MEASUREMENTS ON GRAPH STATES

One appealing property of performing Pauli basis measurements on a qubit within a graph state is that the result is still a graph state with changes to the Clifford side effects of neighbor vertices of the measured qubit in the graph depending on the measurement outcomes. In this work, we require two sequences of measurements: single-qubit Z measurement and two single-qubit X measurements on adjacent qubits in the graph, which we will refer to as XX measurement (as depicted in Fig. 1). These two measurements introduce possible Pauli Z side effects to the resulting graph state. Since only Z side effects are added or removed, it is simple to track the side effects of each vertex with just one bit of information.

The effect of measuring qubit a of a graph state in the Z basis can be described as follows. The vertex a and all edges that connect to a are removed from the graph G. The resulting graph is the graph induced by the subgraph $G - a$. Neighboring vertices of a are affected by a Pauli Z operator if 1 is obtained from the measurement result, as depicted in Fig. 1 (bottom left).

For the XX measurement (single qubit X basis measurements on two connected qubits a and b where they do not share common neighbors), the resulting graph is obtained by removing both qubits a and b from the graph, and the two sets of neighbors of a and b then form a complete bipartite graph (biclique), as shown in Fig. 1 (bottom right). A Pauli Z side effect is added to neighbors of a (b) if the measurement result of b (a) is 1. We note that this is sometimes referred to as data qubit movement or teleportation in the measurement-based quantum computation [50], [51] context and is not the same as joint Pauli measurement typically used in quantum error corrections [52], [53].

Measuring a qubit with Z side effect in the Z basis does not change the measurement outcome since the Z gate and the Z measurement commute. On the other hand, measuring a qubit in the X basis when there is a Z side effect on the qubit flips the result since Pauli Z and X anticommute. These properties are crucial since they affect how the side effects are propagated during the entanglement distribution in the RGS scheme.

We note, that in this article, we use math-type font I, X, Y, Z, or H to represent Clifford operators, particularly

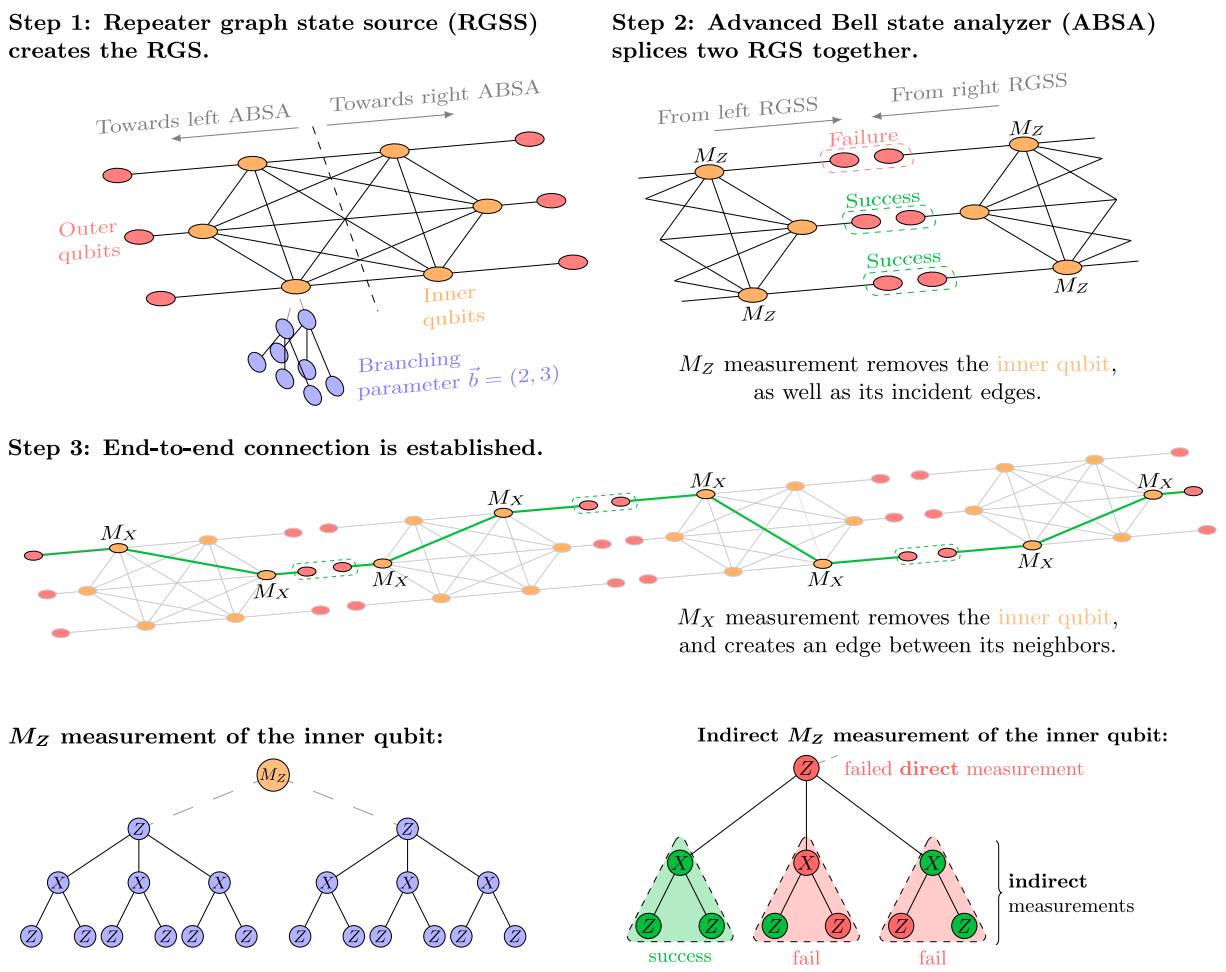

FIGURE 2. Overview of the RGS scheme. The three steps shown here have corresponding actions to the memory-based repeater scheme, where inner encoded qubits correspond to the memories, while outer qubits correspond to the emitted photons. Note that all depicted qubits are photonic. RGS generation in step 1 (at RGSS) mirrors the entanglement swapping of quantum memories but without actually choosing which inner qubits will be paired up. Step 2 (at ABSA) illustrates the link-level generation process through the BSM between each pair of outer qubits. The Z measurement on inner qubits in step 2 and the X measurements in step 3 signify the choosing of which pairs are swapped. Logical measurement of inner qubits in the Z basis is depicted at the bottom. The *Z* and *X* labels inside the blue physical qubits indicate the actual physical measurement bases. For logical X measurement, the Z and X measurement bases of physical qubits are swapped. The indirect Z basis measurement of a physical qubit in the tree encoding is shown in the bottom right. If a direct Z measurement on a qubit fails due to photon loss, the result can still be inferred from the eigenvalue parity of qubits within any of the dotted triangles.

when denoting the Clifford side effects on the qubits of a graph state. In contrast, we use the normal font face X, Y, or Z typically to refer to the Pauli basis of the measurements (e.g., Z measurement or XX measurement).

III. ALL-PHOTONIC QUANTUM REPEATER

In this section, we review the all-photonic scheme proposed by Azuma et al. [25]. We will refer to this scheme as the "RGS scheme" from here onward.

A. RGS SCHEME OVERVIEW

The RGS is made of 2 m inner qubits, forming a complete graph, and 2 m outer qubits, each linked to an inner qubit, where all the qubits are photonic qubits, as depicted in Fig. 2. These inner qubits of the RGS are analogous to the quantum memories in a conventional repeater. The all-to-all connectivity of these inner qubits encodes the entanglement swapping operation, allowing the repeater to select which pair of inner qubits will be swapped to extend the Bell pair. This graph is created locally before the RGS is sent to the measurement devices that establish the elementary links. Thus, the scheme is considered "time-reversed," meaning that the entanglement swap is effectively performed before the link-level entanglement between repeaters is created.

In the RGS scheme, outlined in Fig. 2, there are two network node types. The repeater graph states source (RGSS) nodes and the advanced Bell state analyzer (ABSA) node function similarly to the typical memory-equipped repeaters and the BSA nodes, respectively. To create an end-to-end Bell pair, all the RGSSs between the two end nodes create the RGS. Each RGS is split in half, and each half is then sent to its adjacent ABSA. Photonic Bell state measurements (BSMs)

IEEE Transactions on Quantum Engineering

are performed on every pair of the outer qubits between the two halves of the RGS meeting at each ABSA. A successful BSM between the outer qubits creates an entanglement link between their connected inner qubits. Aside from the two inner qubits that are now connected, single-qubit Z basis measurements are then performed on the rest of the inner qubits, removing them from the system and leaving a linear chain graph state between the two end nodes. Finally, XX measurement is performed on the remaining two inner qubits at each ABSA, creating an end-to-end two-vertex graph state (a rotated Bell pair). Note that the description above looks at the state from the locally equivalent graph state perspective without explicitly tracking the Clifford side effects.

Implementation of the aforementioned measurements depends on the physical encoding of the photonic qubits. For polarization encoding, all required measurements can be implemented with standard linear optics elements, such as half-waveplates, polarizing beamsplitters, and photon detectors [33].

B. LOSS TOLERANCE OF THE RGS SCHEME

The RGS effectively combats photon loss by increasing the number of arms (the parameter m), which in turn improves the probability of obtaining at least one successful BSM and the probability of getting an end-to-end Bell pair. However, blindly increasing the number of arms is not the best approach, as successful measurements of all the inner qubits are needed. Thus, the inner qubits can be encoded in the tree graph state encoding [54], a form of quantum error-correcting code, and logical measurements of inner qubits can be done via a process called counterfactual measurement or indirect measurement [54]. The number of arms m and the branching parameter $\vec{b} = (b_0, b_1, \ldots, b_{n-1})$, which describes the tree encoding, together determine how much loss and error the RGS can tolerate. An example of the tree-code-encoded inner qubits with $\vec{b} = (2, 3)$ is shown in Fig. 2.

C. LOGICAL MEASUREMENT OF INNER QUBITS

The logical measurement of inner qubits can be achieved by performing single-qubit measurements on all of the physical qubits in a predecided pattern, where the qubits in the same level of the tree undergo the same basis of measurements (depicted in Fig. 2). For the X (Z) basis measurement, perform the X (Z) measurement on the first level of the tree and alternate into the Z (X) measurement on the second level. Basis alternation occurs at every level, meaning that for the X (Z) basis measurement, the X (Z) measurement is done on the odd level, while the Z (X) measurement is done on the even level.

The concept behind the counterfactual measurement stems from the fact that graph states can be described using the stabilizer formalism. The measurement result of qubit a, which is part of the support of the stabilizer generator g_i, recall (2), can be deduced if all other qubits in the generator g_i were successfully measured (either directly or indirectly). Therefore, the Z measurement result of qubit a at level k can be deduced if any of its neighbors b at level $k+1$ are successfully directly measured in the X basis and all of N_b in level $k+2$ are also successfully measured in the Z basis (either directly or indirectly). This example is shown in Fig. 2 (bottom right) as the stabilizer generator defined from each of the second level vertex corresponds to the measurement patterns.

The logical measurement results of the inner qubits can be inferred from finding the eigenvalue parity of a specific set of obtained physical results. For Z basis measurements, the logical outcome is determined by the parity of eigenvalues across all qubits in the first level. Conversely, for X basis measurements, the logical outcome is determined from the parity of the eigenvalue resulting from the X measurement of qubit a in the first level and the eigenvalues of its neighbors measured in the Z basis in the second level (either direct or indirect). In scenarios involving only photon losses, all the logical results deduced from any qubit in the first level and their neighbors are all identical. For proof of how the parity of these groups of qubits signifies the logical result, we refer readers to the supplementary material of [25].

D. OPERATIONAL ERROR TOLERANCE OF RGS

The tree encoding also offers tolerance to quantum operation errors. To correct physical measurement results of qubits in the tree, only those measured in the Z basis can be corrected. This is done by performing a majority vote on the indirect measurement results of the qubit as mentioned in the prior subsection for correcting qubit loss.

For the logical results, only the inner qubits measured in the X basis can be corrected. Similar to the physical qubit case, a majority vote is performed on the X measurement results of all qubits in the first level, as only one is needed to deduce the logical result. This is in contrast to the logical Z, which necessitates success across all Z measurements (either direct or indirect) in the first level. These properties imply that the capacity to tolerate errors also depends on the loss probability of photons.

E. TRANSMISSION ORDER OF PHOTONS IN THE RGS

The measurement basis selection of the inner qubits is dependent on the BSM outcome of the outer qubits. As long as the outer qubits arrive at the ABSA before their connected inner qubit, the measurement basis can be determined locally at ABSAs. The physical qubits composing the inner qubits can be sent in any order as long as it is known to the ABSA beforehand. This is fixed and does not require any delay line to correct the ordering in our work, as we will show in the generation sequence in Section V. We note that even if the photons are lost, assuming that the photons are well separated temporally, the ABSA can deterministically flag the loss event. This well-separated assumption is also commonly adopted in memory-based repeater schemes for multiplexing photons from multiple memories into a single fiber [55].

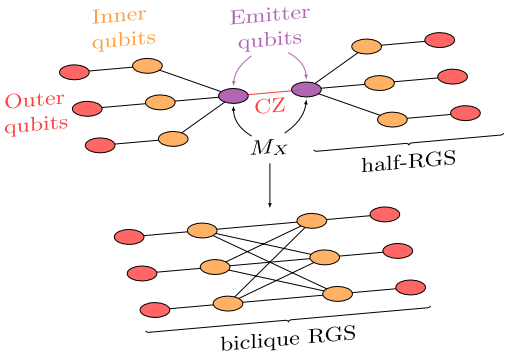

FIGURE 3. Example of half-RGS and the transformation of two half-RGSs into a biclique RGS. The anchor emitter qubits of the two half-RGSs are joined via an application of a CZ gate followed by the XX measurement resulting in a biclique RGS.

IV. HALF-RGS BUILDING BLOCK

The complete graph connectivity of inner qubits in the RGS is not a strict requirement to encode the entanglement swap. If each half of the inner qubits is connected into a complete bipartite graph (biclique) as depicted in Fig. 3, this is enough to be used as the RGS [56], [57]. It was recently shown that the complete graph of inner qubits can also be a disadvantage, limiting the end-to-end rate when loss is not too high [58]. From here on, we will refer to this biclique RGS also as the RGS when it is unnecessary to differentiate them.

In this section, we present our first contribution, the half-RGS, which we use as our building block to create the biclique RGS. It bridges the end nodes and RGSS disparity and also allows seamless integration between memory-based repeaters and RGS-based repeaters.

A. HALF-RGS DESCRIPTION

The half-RGS is depicted in Fig. 3. The purple qubit, which we refer to as the "anchor qubit," denotes an emitter (or a stationary memory qubit) acting as an anchor to half of the photonic RGS. Joining two half-RGSs at the anchors via a CZ gate and performing the XX measurement (equivalent to performing a Bell measurement) results in the RGS, hence the name half-RGS. Next, we show that some of the previously open problems for the RGS scheme [41] can be addressed by utilizing the half-RGS building blocks.

B. IMPROVING RESOURCE REQUIREMENT AT END NODES

The incorporation of end nodes into the RGS scheme has not been explored aside from QKD applications, where end nodes are measurement nodes rather than full compute nodes. The main difference in having compute nodes as opposed to measurement nodes is the requirement that compute nodes need to have quantum memories storing the states and wait for all the measurement result messages from ABSAs and RGSSs to arrive before the Bell pairs are ready for use. One way to realize this was explored [28] (depicted at the top of Fig. 4), where the end nodes are equipped with at least m (the number of RGS arms) quantum memories, and for one trial, m memories emit photons to meet with half-RGS at an ABSA.

In the approach outlined in [28], achieving correctable Bell pairs for applications beyond QKD while fully utilizing the RGS scheme's rapid trial time requires end nodes to have an additional rm memories in reserve, since photons for the previous r trials are already emitted from all the memories while still waiting for the correction messages to arrive. Here, r denotes the ratio of the time required for the classical message to travel from the farthest ABSA and the RGS generation time. A rough calculation suggests that for a separation distance of 1000 km, end nodes would require approximately 150 memories, based on the analysis presented in [27], to maintain pace with the trial rate ($r = 10, m = 15$). The value of r, and consequently the number of required buffer memories, increases with the end-to-end distance and with faster RGS generation rates.

In contrast, our proposed architecture (shown at the bottom of Fig. 4), leveraging the half-RGS building block, streamlines this requirement by necessitating only r quantum memories and $|\vec{b}| + 1$ emitters (where $|\vec{b}|$ denotes the depth of the tree encoding at each end node) resulting in a total of $r + |\vec{b}| + 1$ combined memories and emitters. The r quantum memories, unlike emitters, do not need to emit photons, provided that the qubit state of the anchor emitter of the half-RGS is swapped into these quantum memories. The emitters also do not need to have coherence time as long as quantum memories do, since their role is to assist in generating the photonic qubits in the half-RGS. This configuration effectively doubles the trial rate compared to the rm-memory (or $2rm$ when employing multiplexed fiber to match our achievable rate) approach in [28]. The difference in the architectures is illustrated in Fig. 4.

To quantify this resource comparison, the architecture in [28] requires a total of rm emissive memories. In contrast, our approach requires only $r + |\vec{b}| + 1$ combined memories and emitters, offering substantial savings for typical reasonable RGS parameters that optimize the distribution rate (e.g., $m > |\vec{b}| + 1$). The fundamental improvement is that our architecture's resource requirement scales additively with the round-trip factor r, rather than multiplicatively, which significantly reduces the memory overhead for long-distance communication.

C. INTEGRATION WITH MEMORY-BASED REPEATERS

In light of our current discussion, it is more appropriate to view the RGS scheme as a link-level connection between two memory-equipped nodes rather than as repeater nodes at the network level, as shown in Fig. 5. The RGS scheme can connect any two nodes, not just end nodes. The Bell pairs it creates function as link-level resources, similar to those generated by other link architectures, such as Memory–Interference–Memory, Memory–Memory [24], Memory–Source–Memory [59], or Sneakernet links [60], and can be allocated to the quantum nodes' resource

IEEE Transactions on Quantum Engineering

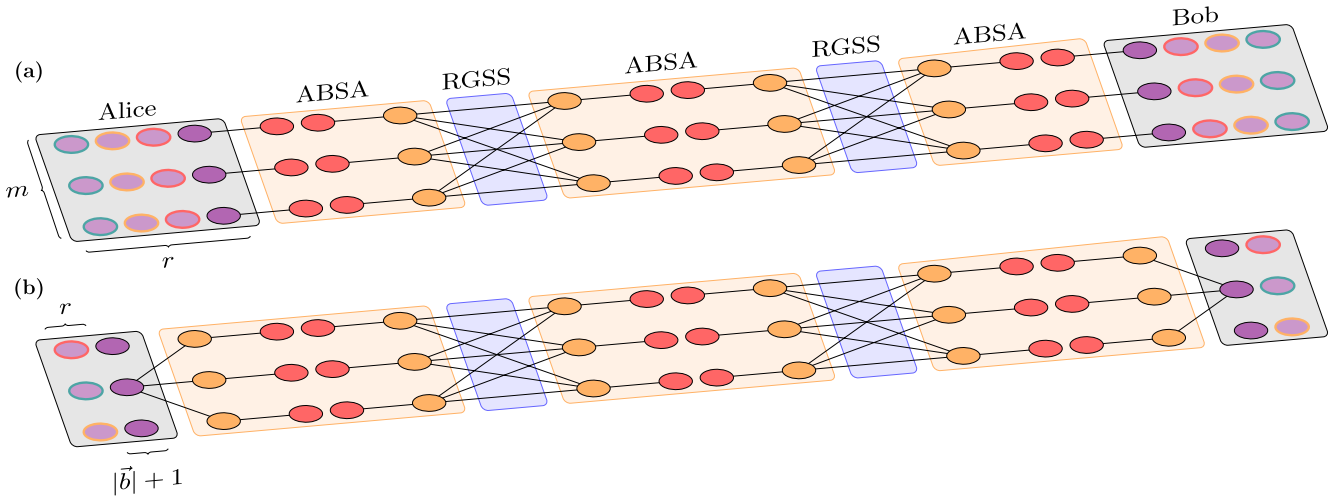

FIGURE 4. Architectures supporting the RGS scheme where the photonic states generated at end nodes are different. (a) Architecture proposed in [28], where end nodes require *m* emissive memories for each trial, along with *rm* idle memories that have already been utilized in prior trials and are awaiting messages from all ABSAs. (b) Proposed architecture, featuring end nodes equipped with half-RGS building blocks. In this setup, end nodes require $|\vec{b}|+1$ quantum emitters (where $|\vec{b}|$ represents the depth of the tree encoding plus one), while reserving *r* memories awaiting notification messages from prior trials. Purple circles with black borders represent the quantum emitters utilized in the current trial. Purple circles with colored borders in both (a) and (b) indicate idle memories awaiting messages from ABSAs, with the same colors denoting memories participating in the same trials.

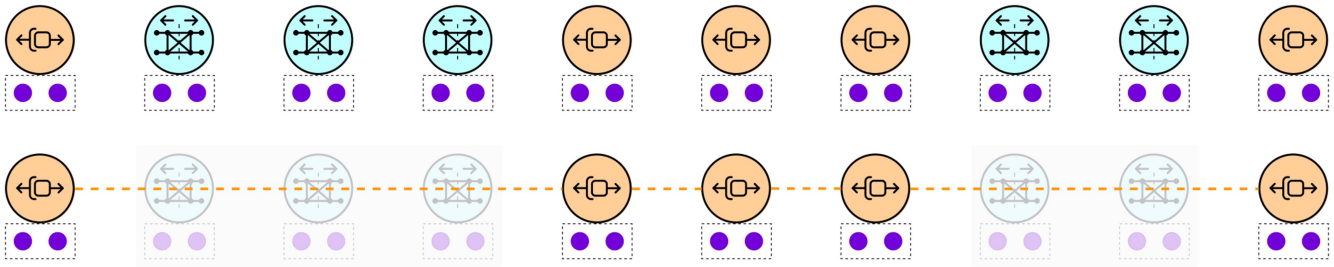

FIGURE 5. Segments constituting RGSS (in light blue) and ABSA (omitted) nodes are treated as virtual links to memory-equipped repeaters (orange). The RGS scheme link is invisible at the connection level protocol, reducing the cost of connection setup and management.

management software. This is in the spirit of the heterogeneity and interoperability goals of the future Quantum Internet [55]. By abstracting the RGS repeater chain as a virtual link, the complex process of photonic state generation, measurement, and correction is encapsulated within the link layer of a layered network architecture [61], [62]. Consequently, event-driven network layer protocols [55], [63], [64] can manage this virtual link using the same established rules for resource allocation and scheduling as conventional memory-based links, greatly simplifying the network control plane and enhancing modularity.

D. TIMING SYNCHRONIZATION

The original RGS scheme requires that the outer qubits from both sides arrive at the ABSA nearly at the same time, within an indistinguishable time window, for the entanglement swapping via BSM to work. Since we separate the two halves of RGS to be generated by a different set of emitters, the timing message only needs to be exchanged between neighbors and the controller, which controls the emitter at each link in the same way as for conventional memory-based repeaters. This is unlike the case where the whole graph is generated by one set of emitters [27], [29]. In the single-set case, the timing message must be sent to both left and right nodes to achieve the required coordination along the entire connection path (implying a global clock or optical delay lines), a significant complication in engineering [65] that our building block simplifies.

Although this necessitates end nodes to be equipped with a half-RGS generation device, as it is the same component as the RGSS, it is not unreasonable to require it. A more end-node friendly approach would be for end nodes connected to a repeater bridging the RGS scheme and the port connecting to end nodes to be memory based.

V. GENERATION OF HALF-RGS

The generation of RGS is often the most difficult part in realizing the RGS scheme. Various generation methods have

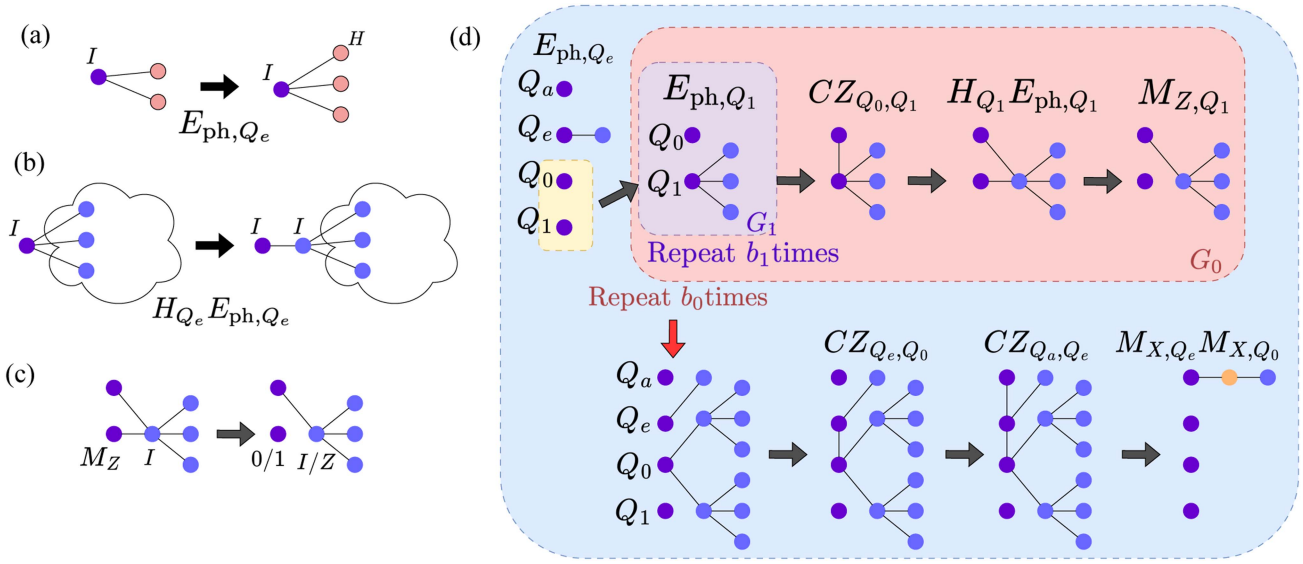

FIGURE 6. (a) Emission of a photon with side effect labeled. (b) Pushout operation, photon emission followed by a Hadamard gate. This operation does not introduce any side effect. (c) Side effect of pushout followed by a Z measurement. This is the main sequence used in generating the half-RGS. (d) Sequence (modified from [27]) to generate one arm of half-RGS with $\vec{b} = (2, 3)$. This needs to be repeated m times to create m arms.

been proposed [25], [29], [30], [66], [67], along with optimization techniques building on top to reduce resources and time [31], [32], [68]. Here, we take the approach proposed in [29] for deterministically generating photonic graph states via quantum emitters.

A. ASSUMPTIONS ON THE OPERATIONS

Assumptions about the quantum emitters and their operations are as follows (also shown in Fig. 6). Quantum emitters are arranged in a linear topology $(Q_a, Q_e, Q_0, Q_1, Q_2, \ldots, Q_{|\vec{b}|-1})$, where Q_a is the anchor qubit for the half-RGS, and Q_e is the emitter for outer qubits. Recall that we use the term anchor qubits to refer to the emitter that is part of the half-RGS anchoring the photonic qubits (see Fig. 3). Hadamard gates can be applied on individual emitters, as well as controlled-phase gates between neighboring ones. Photon emission is modeled using a controlled-not gate to a new qubit initialized in $|0\rangle$ [see Fig. 6(a)]. In addition to the manipulation rules of graph states mentioned previously, we also require pushout operations, where the emitter qubit in the graph state is replaced with the newly emitted photon, and the emitter is now connected to only the new photon [69], [70]. This is achieved by photon emission followed by a Hadamard gate, as depicted in Fig. 6(b).

BSM using linear optics that is used in our protocol is equivalent to first applying a controlled-phase gate on the two qubits followed by an XX measurement. Success probability of the BSM is bounded by 50% due to the inability of linear optics to reliably distinguish two of the four possible measurement outcomes. We model this by taking odd-parity measurement outcomes (either 0/1 or 1/0) as success. This choice is arbitrary, and any two of the four outcomes would work.

B. SEQUENCES FOR GENERATING THE HALF-RGS

The sequence of generating half-RGS with m arms and branching parameter $\vec{b} = (b_0, b_1, \ldots, b_{n-1})$ anchored at Q_a on one side, a modified version of [27] and [29], is given as follows [also depicted in Fig. 6(d)]:

$$\left(M_{X,Q_e} M_{X,Q_0} CZ_{Q_a,Q_e} CZ_{Q_e,Q_0} G_0^{b_0} E_{\mathrm{ph},Q_e}\right)^m$$
$$\text{with } G_k = M_{Z,Q_{k+1}} H_{Q_{k+1}} E_{\mathrm{ph},Q_{k+1}} CZ_{Q_k,Q_{k+1}} G_{k+1}^{b_{k+1}}$$
$$\text{and } G_{n-1} = E_{\mathrm{ph},Q_{n-1}} \tag{4}$$

where E_{ph,Q_i} and M_{P,Q_i} denote photon emission and measurement in the P basis on emitter i, respectively. Joining two half-RGSs into an RGS can be done by performing CZ between Q_a on the left and right sides and performing the XX measurement.

In contrast to the generation sequences and analysis presented in [27], our approach requires twice the number of emitters per RGSS and an additional two emitters dedicated to the generation of outer qubits. However, our method achieves a reduction in generation time, halving the previous duration, and eliminates the need for delay lines or efficient photon storage at ABSA as required in prior works [27], [28], [29], [31]. This lowers the probability of outer qubits being lost in the fiber, as all photons are generated in the order of measurements to be performed.

C. SIDE EFFECTS CREATED DURING THE GENERATION

Both the generation of half-RGS via the quantum emitters at the RGSS and the measurements done at ABSA can introduce Clifford side effects to the state. Tracking and correcting these side effects are crucial to ensure that the Bell pairs formed between the two end users of the connection are in the desired state.

From the half-RGS generation sequences, shown in Fig. 6, the physical qubits at the lowest level (leaf nodes) of the inner qubits and the outer qubits will have an H side effect [see Fig. 6(a)]. However, these side effects can be removed via optical Hadamard gates applied to the photons before they are sent out to the ABSA or by swapping the measurement basis between Z and X at the ABSA. On the other hand, the remaining physical qubits in the tree may have a Z side effect introduced with a probability of 50% each, as they are generated via the pushout operation followed by the measurement of its neighbor emitter [see Fig. 6(c)].

Furthermore, the outer qubits are also subject to possible Z side effects resulting from the XX measurement connecting them to their respective inner qubits.

Both the joining of two half-RGSs into a biclique RGS and the joining of outer and inner qubits involve performing a controlled-phase gate on the two emitters followed by an XX measurement, depicted in the last step of Figs. 3 and 6(d), respectively. These XX measurements may also toggle the Z side effects on all the physical qubits in the first level of the tree (where the effect was shown in the bottom right of Fig. 1). Two approaches are possible to track this: tracking the logical Z side effect on the inner qubit itself, and toggling the side effects of physical qubits between Z and I. We will first utilize the latter view for the general generation-agnostic protocol in Section VI-B and the former view when we outline the protocols specific for our half-RGS construction in Section VI-C.

VI. FULL RGS PROTOCOL

We now describe the communication protocol to realize the RGS scheme given our assumptions discussed above. First, we will describe a biclique RGS generation agnostic protocol outlining where information about measurement and side effects originates and how it should be passed to intermediate and end nodes. Later, in the next section, we will go into the generation specific with our proposed half-RGS interface leveraging graph state manipulation rules to argue about the calculations of Pauli frame corrections.

A. OVERVIEW

For each trial, every RGSS generates and sends an RGS to their adjacent ABSA, followed by a classical message containing all the side effects of each physical photonic qubit. The side effect information from the generation process is always available to the RGSS independent of how the RGS is generated [25], [29], [30], [31], [66]. At each ABSA, BSM is performed on the outer qubits followed by measurements on the inner qubits determined by the BSM outcomes. Note that ABSAs need to know the set of possible side effects that can occur on the physical qubits in order to measure them in the right basis (e.g., Y basis measurement should be used instead of X on the first level of tree encoding if side effect is introduced via Y measurement of the emitter as in [27] for complete graph RGS); thus, adjacent pairs of RGSS and ABSA need to communicate them in advance.

For each arm of an RGS, ABSA creates a tree of measurement results, depicted in Fig. 7, recording the results of the measurements and the measurement basis, or whether the photon was lost. This tree is analogous to the tree encoding logical qubit. The logical measurement results of each inner qubit can then be locally determined at the ABSA by processing all the measurement trees and the side effect information received. The propagation of the Z side effect to neighbor nodes and eventually to end nodes can be reduced down to two bits denoting whether the logical X result of the inner qubits of the neighbor ABSA should be flipped or not. One more bit of information is also sent to each end node, denoting the success or failure of trial at each ABSA. Finally, the end nodes determine the correction operation required to correct the memory held into an end-to-end two-vertex graph state that is equivalent to a Bell pair.

B. GENERATION-AGNOSTIC PAULI FRAME CALCULATIONS

Although the photons are measured in the order that they arrived at the ABSA, conceptually, we can think of them being measured in any order as long as each outer qubit is measured before its corresponding inner qubits. We now describe how the Pauli frame corrections can be calculated for the memories at the end nodes. Fig. 7 outlines the following procedure.

First, we assume that success or failure of all BSMs on the outer qubits is known; thus, all the measurement bases for inner qubits have been decided. Before we begin tracking the state changes due to measurements, ABSAs construct a measurement tree for each inner and outer qubit pair of each RGS arm with the side effect information about all the physical qubits received from RGSS and end nodes. The measurement tree stores the measurement basis and its result or marks that the qubit is lost. This is denoted by + (for 0) or − (for 1) with the measurement basis (X or Z) for successful measurements and L for loss. If the qubit has a Z side effect from the generation, shown as a yellow filled vertex in Fig. 7, the measurement result in the X basis will be toggled, while those measured in Z and lost events L stay the same.

Next, we propagate the BSM results obtained from the outer qubits to their inner neighbors, as shown in Step 2 of Fig. 7. BSM has the same effect as an XX measurement in Fig. 1 and can create a Z side effect. Successful BSM outcomes propagate to the inner qubits across the RGSs, as shown by the black arrows in Step 2. If the measurement outcome on the outer qubit from the left (right) side is 1 (1X in the figure), the measurement results of the physical qubits

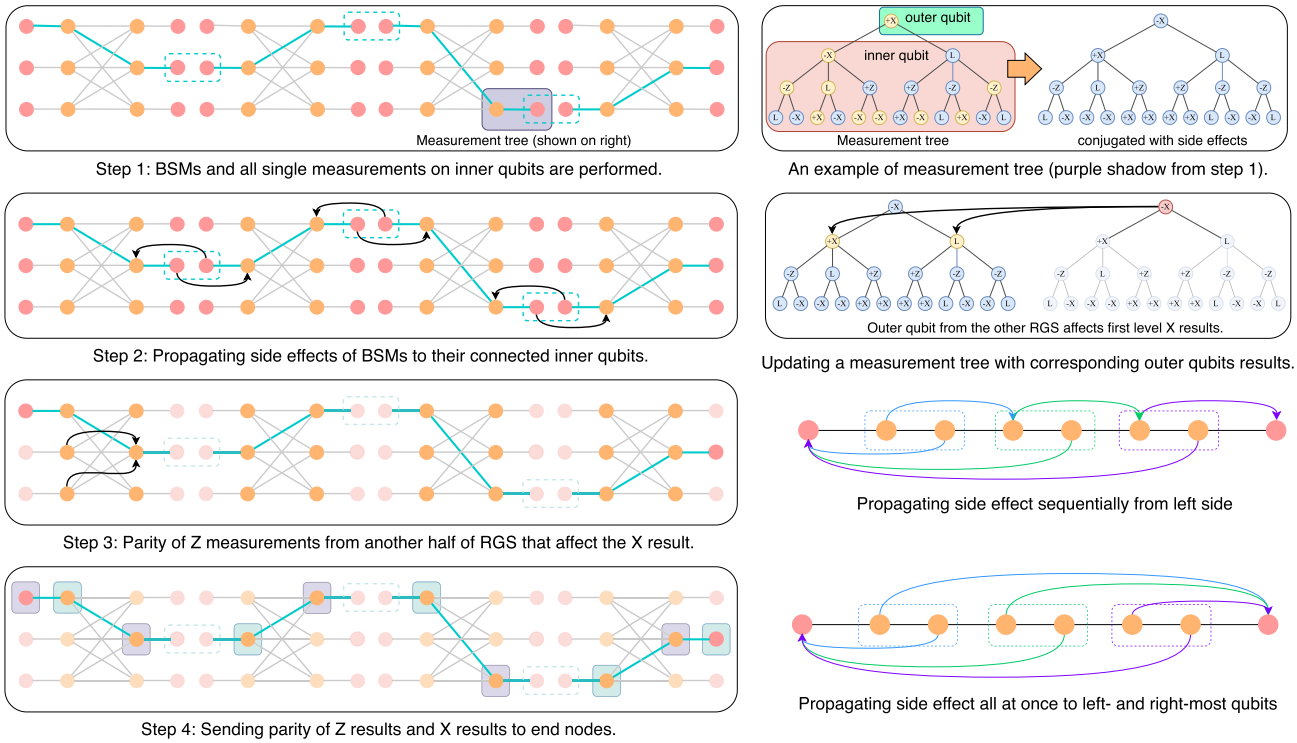

FIGURE 7. Tracking of side effect propagation at each step, the resolution of physical and logical measurement results, and the rationale behind the Pauli frame corrections applied at end nodes, as illustrated in Steps 1–4 on the left-hand side of the figure. Examples of measurement trees and their updating during the Pauli frame calculation process are presented in the top two panels on the right side. Yellow filled vertex represent that the vertex has a Z side effect. The sequential propagation of side effects, viewed hop-by-hop, is contrasted with an equivalent view of simultaneous propagation to the outermost qubits, depicted in the bottom two panels on the right side.

in the first level of the right (left) tree are flipped. We do not need to consider the Z propagation to inner qubits if their outer neighbors were part of a failed or discarded BSM since we will measure these inner qubits in Z and the Z side effect does not change Z measurement results.

The results of the Z measurements on the inner qubits of the same RGS affect the X measurement results of that RGS. However, such measurements are performed at a different ABSA, making their outcomes locally unavailable. This is shown in Step 3 in Fig. 7. Fortunately, we can see from the bottom two panels on the right-hand side of Fig. 7 that the Z propagation of XX measurements can be processed once at end nodes via the parity product of the measurement results. This implies that the Z side effect, possibly occurring from all the inner qubits that have undergone Z measurements, can be dealt with in the same way. ABSAs compute partial parity of locally performed Z measurements, given by the product of the measurement outcomes, and send this information to the end nodes, where it is processed to yield the total parity.

Therefore, each ABSA needs to send only two bits of information to the end nodes per trial; one bit denoting whether the Z is propagating to that side of end nodes or not (parity of measurement results), and whether the procedure is successful. The number of classical bits that each ABSA receives is the same as the number of total photons. This is in agreement with the two-stage protocol analysis made in [41].

C. HALF-RGS-SPECIFIC PAULI FRAME CALCULATION

In this section, we describe how utilizing our proposed half-RGS building block generated by quantum emitter can facilitate Pauli frame correction calculation and later leading to simple graphical aid to calculate the end-to-end fidelity of the protocol. Similar to the generation-agnostic protocol, we still perform the first step of Fig. 7, but the procedure after the first step will be different.

With the way we construct half-RGS building blocks, all the photons are generated in the same order they are sent and measured at an ABSA without the need for an optical delay line. Specifically, we can see that each arm of the half-RGS is created sequentially. This allows us to track and propagate the Z side effects of each generated arm to the anchor qubit of half-RGS one by one during the generation process. Note that the half-RGS anchor qubit never emits photons and the only operation performed on it is the CZ (without the joining to create biclique RGS that performed last), which commutes with Z side effects; thus, treating the side effects and tracking them this way is sound.

First, let us define the qubits involved in this one-hop picture, as shown in Fig. 8 (this is the second to last step of Fig. 6 where the physical qubits of tree encoding is shown as logical orange qubit instead). Let Q_a^L, Q_e^L, Q_0^L, Q_{out}^L, and Q_{in}^L be the anchor qubit of the half-RGS, emitter for outer qubits, anchor of the inner logical qubits, outer qubit, and inner

IEEE Transactions on Quantum Engineering

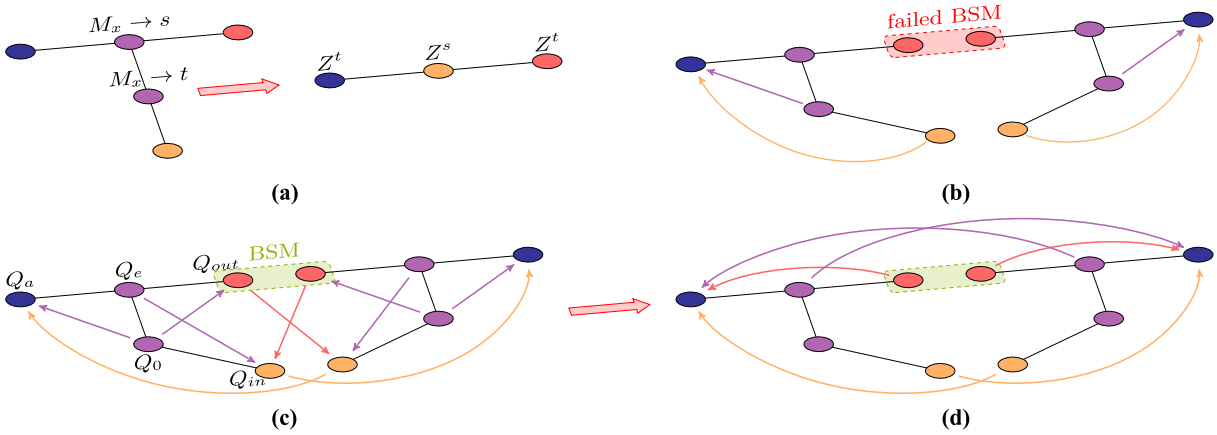

FIGURE 8. Side effects propagation for an arm of one-hop RGS link from half-RGS. An arrow pointing from *a* to *b* denotes that if measurement results of *a* is 1, the measurement results of *b* should be flipped. (a) Side effect propagations of creating an arm attaching to the anchor qubits by performing XX measurements on the emitters joining inner and outer qubits. (b) Propagation for failed or discarded BSM case where inner qubits are measured in the Z basis. (c) Side effect propagations of the successful BSM arm, where inner qubits are measured in the X basis. (d) Simplified version of (c) where the tips of the arrows are moved to anchor qubits by following the chain of arrows.

logical qubit for the left-hand side coming to the ABSA, respectively. Similarly, Q_j^R denotes the same qubits for the right incoming qubits.

Recall the side effects introduced by the generation sequence of the half-RGS described in Section V-C. Graphically (depicted in Fig. 8), if measuring a qubit according to the RGS protocol can introduce side effects (flipping the measurement result) to other qubits upon obtaining "1" as the measurement result, we draw arrows from this qubit to the affected qubits. We note that the arrows going from inner and outer qubits are the results of viewing the last step of Fig. 6 when Q_1 and Q_2 are already measured out, while arrows going out from Q_0 and Q_1 are derived from the generation sequence, the last step of Fig. 6 where inner and outer qubits are moved from the previously connected emitters to become an RGS arm attached to the anchor. The figure shows two measurement patterns: the case where inner qubits are measured in the X basis (left) and the case where they are measured in the Z basis (right). From this graphical picture, we can realize that a single measurement flip on one qubit propagates through the chain of arrows and always affects one of the anchor qubits. This allows us to simplify the effect of each measurement to always flipping the Z side effects of only the anchor qubits (lower half of Fig. 8).

By repeating this for every arm of the one-hop RGS link between the two half-RGSs, Pauli frame corrections for one-hop RGS link can be calculated. To go from one-hop to multiple-hop linear chain of the RGS link, recall that at each RGSS node, the two halves of half-RGS are joined and combined into a biclique RGS by performing a CZ gate followed by XX measurements. Since the Z side effect tracked for the one-hop picture commutes with CZ and flips the result of X measurement, we will need to flip reported measurement results if the anchor had the Z side effect tracked on it. This measurement results then sent to end nodes to be postprocessed also indicate the Pauli frame corrections similarly to Step 4 of Fig. 7.

D. PROTOCOL VALIDATION VIA SIMULATION

To support the analytical derivations of the Pauli frame corrections for both the generation-agnostic and half-RGS protocols, we performed numerical simulations using the stabilizer tableau simulator Stim [71]. We simulated our protocols for a range of RGS parameters—including various logical tree-encoding depths (from unencoded to 5) and a number of arms (m) ranging from 1 to 20—using a simulation code that allows for arbitrary user-defined values for these parameters and the total number of hops. In the generation-agnostic simulation, each physical qubit forming an inner qubit is prepared from quantum circuits using Hadamard and CZ gates without measurements. To simulate the stochastic Z side effect on each physical qubit within an inner logical qubit, a Z gate is applied with 50% probability after state generation. Subsequently, inner–outer qubit arms are generated following the procedure in Section V until half-RGSs are obtained and transformed into biclique RGSs. Once all RGSs are generated at each RGSS, along with the two half-RGSs from the end nodes, BSMs are performed on all outer qubit pairs, and measurement bases are selected for all inner qubits. Finally, all physical qubits in the system are measured simultaneously in a single circuit layer.

Instead of directly simulating message passing, the correction procedure is executed step by step, as outlined in Section VI-B. For each RGS arm, a measurement tree is created, followed by updating the measurement tree with side effect information and Z propagation from the BSM and the decoding of the logical result. Finally, the 4 bits of information at each ABSA are processed, and correction operations are applied to the end nodes' memories accordingly.

For the case where biclique RGS is created via our proposed half-RGS building blocks, we simulate it hop-by-hop similarly to the description in Section VI-C. This helps speed up the simulation as the total number of qubits during the simulation is bounded by only a single hop independent of how many hops we want to simulate. All the photons are generated exactly as described in Section V, photon-by-photon, confirming that our Pauli frame calculation and also the generation sequence create the right state.

To confirm that the final state between two end nodes is a two-vertex graph state without any side effect, we used Stim to examine the stabilizer generators of the final two qubits. We verified that the generators are X_aZ_b and Z_aX_b as expected, where the subscripts a and b denote the qubit held by Alice and Bob, respectively. Simulating the photon loss event is achieved by probabilistically marking qubits as lost with some probability. If a qubit is marked as lost, we randomly apply Pauli X, Y, or Z before the measurement, and the results are then removed from the measurement tree, excluding their participation from the logical qubit decoding process.

VII. FIDELITY OF THE END-TO-END BELL PAIRS

The fidelity of end-to-end Bell pairs is one of the most important measures that characterizes the states created in a quantum network. In this section, we derive this fidelity by analyzing the error probabilities on a single-hop link, which can then be extended to the full end-to-end path. Our derivation relies on the graphical framework for Pauli frame corrections established in our earlier discussion and illustrated in Fig. 8.

A. ERROR MODELING AND DECOMPOSITION

Our analysis assumes that errors manifest as independent single-qubit Pauli channels on each photonic qubit. For simplicity, and in line with standard approaches [25], [27], [28], we consider the quantum emitters, gate operations, and measurement devices to be ideal. This is a reasonable simplification, as noise from these components can be modeled as an effective noise channel on the photons themselves [72].

While a standard analysis of Bell pair errors often applies Pauli errors (X, Y, or Z) to a single qubit due to the symmetry of Bell states, we adopt an equivalent viewpoint specific to the graph state formalism. We track only the Z-type errors that accumulate on each of the two end-node qubits, which simplifies error propagation across multiple hops without any loss of generality. As shown in Fig. 9, this approach is equivalent to the standard model up to stabilizer transformations; a Pauli X, Y, or Z error on one qubit corresponds to a Z error on the other, Z errors on both, or a Z error on the original qubit, respectively.

A key idea in our derivation is to decompose the single-hop error probability into two distinct contributions: 1) errors from inner qubits, which introduce independent Z errors to each end node, and 2) errors from outer qubits, which can induce correlated errors across the link. Because the effects of the inner-qubit errors can be accounted for at the end of the protocol, we can first analyze the correlated errors from the outer qubits and then apply the independent inner-qubit error channel to the result.

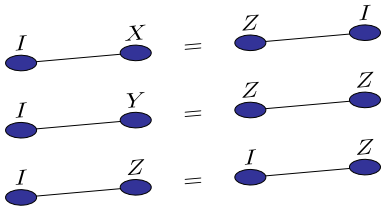

FIGURE 9. Equivalence descriptions of graph states with side effects. The graph states on the left-hand side are normally used to represent Bell pairs with *X*, *Y*, and *Z* Pauli errors while the right-hand side is what we used in this article for when error occurs.

B. ERROR CONTRIBUTION FROM OUTER QUBITS

We first analyze how errors from operations on the *outer qubits* contribute to the effective error on the Bell pair after entanglement swapping. These qubits participate in BSMs that connect adjacent half-RGS segments. The error analysis for this process follows the standard treatment for memory-based entanglement swapping. Each outer qubit is subject to an independent Pauli error channel, and we represent the state of a link with a four-element probability vector $\mathbf{e} = [w, x, y, z]^T$, corresponding to the probabilities of an ideal Bell pair (II) or a pair with an effective ZI, ZZ, or IZ error, respectively.

When a BSM is performed between two links with error vectors $\mathbf{e_1}$ and $\mathbf{e_2}$, the output error vector is computed via the transformation given by

$$\mathrm{BSM}(\mathbf{e_1}, \mathbf{e_2}) = \begin{bmatrix} w_1w_2 + x_1x_2 + y_1y_2 + z_1z_2 \\ w_1x_2 + x_1w_2 + z_1y_2 + y_1z_2 \\ w_1y_2 + y_1w_2 + x_1z_2 + z_1x_2 \\ w_1z_2 + z_1w_2 + x_1y_2 + y_1x_2 \end{bmatrix}. \quad (5)$$

For our one-hop picture, the BSM occurs between two stationary emitter–photon pairs. Assuming that the emitter is initially error-free, the error vector for each pair is determined solely by the channel noise on its corresponding outer photon. This transformation can be applied iteratively to compute the final error vector across a multihop path, since the process of joining two half-RGSs is also a BSM, in this case between emitter–emitter pairs.

C. ERROR CONTRIBUTION FROM INNER QUBITS

The error contribution from inner qubits arises from physical errors that flip measurement outcomes, which, in turn, cause an incorrect Pauli frame correction to be tracked at the half-RGS anchor. An error is applied to the final state at an end node if an odd number of such physical errors occurs on the measurement results that influence its corresponding anchor qubit, as depicted in Fig. 8.

We assume that all RGSSs and ABSAs are equidistant and that error parameters are equal for every hop for the moment,

but the derivation below is general and can be adapted to arbitrary setting. Let p_{ZI} and p_{IZ} denote the probability that a one-hop RGS link between two half-RGSs has Z error on the left and right anchor (or memory), respectively. Suppose that there are N hops between the two end nodes; the end-to-end probability that Alice's (left) memory has Z error is given by

$$p_{ZI}^{\text{e2e}} = \sum_{k\ \text{odd}}^{N} \binom{N}{k} p_{ZI}^{k} (1-p_{ZI})^{N-k} \tag{6}$$

$$= \frac{1}{2}\left(1-(1-2p_{ZI})^{N}\right) \tag{7}$$

and similarly for Bob's (right) side by

$$p_{IZ}^{\text{e2e}} = \sum_{k\ \text{odd}}^{N} \binom{N}{k} p_{IZ}^{k} (1-p_{IZ})^{N-k} \tag{8}$$

$$= \frac{1}{2}\left(1-(1-2p_{IZ})^{N}\right) \tag{9}$$

assuming that p_{ZI} and p_{IZ} are smaller than 0.5, a reasonable assumption for end-to-end Bell pairs to not be a completely mixed state.

The single-hop error probabilities, p_{ZI} and p_{IZ}, contributed by the inner qubits are given by

$$p_{ZI} = p_{IZ} = \frac{1}{2}\left(1-\left(1-2p_{\text{in}}^{X}\right)\left(1-2p_{\text{in}}^{Z}\right)^{m-1}\right), \tag{10}$$

where p_{in}^{P} denotes the probability that a logical measurement in basis $P \in \{X, Z\}$ on a tree-encoded inner qubit is decoded incorrectly. This logical error probability can be derived from underlying physical error parameters, as detailed in analyses such as [27].

D. COMBINED FIDELITY

To find the final fidelity, the two error contributions are combined. First, one calculates the error vector resulting from the outer-qubit BSM chain. Then, the independent error channel due to the inner qubits, described by probabilities p_{ZI}^{e2e} and p_{IZ}^{e2e}, is applied to this vector. The fidelity is the final probability of the ideal Bell state component, the II component.

A direct consequence of this derivation is that the final error channel is biased. While outer-qubit operations contribute to all error terms (ZI, IZ, ZZ), the inner-qubit measurements only contribute to the independent ZI and IZ terms. Therefore, under isotropic noise, the RGS scheme will produce errors that are biased toward the ZI and IZ channels over the ZZ channel.

This analytical approach to error flipping and tracking is analogous to techniques used in prior works [63], [73], [74] for simulating purification protocols, as well as the flip simulator of Stim [71]. Leveraging this insight, we conducted Monte Carlo simulations to evaluate the error probability of inner logical qubits across different branching parameters. We found that the results align with the average error model derived in [27].

VIII. DISCUSSION

In this article, we proposed a practical communication protocol for the implementation of the all-photonic RGS scheme introduced by Azuma et al. [25], alongside an architectural framework leveraging the half-RGS building block to generate the photonic graph states. All-photonic repeaters have so far been limited to QKD applications only. Our proposed architecture addresses this drawback and extends the relevance of all-photonic repeaters to encompass scenarios requiring a corrected Bell pair as the ultimate resource. This is achieved by integrating memory-equipped end nodes into both the protocol and architecture. This integration allows seamless incorporation of our approach into conventional memory-based repeater networks, consistent with the architectural principle of a quantum internet in [55], treating segments between memory-equipped nodes connected via all-photonic repeaters as virtual physical links at the same abstraction with existing memory-based link architectures.

We provide a general framework for computing the required Pauli frame corrections in a way that is agnostic to the RGS generation scheme. Our approach relies on a set of graphical rules that simplify the calculation of the final Clifford side effects that affect the end nodes. We propose the half-RGS as a base building block for our architecture along with a scheme for its generation. Applying our general Pauli correction framework, we present a detailed communication protocol that specifies what bases the qubits need to measure in and what information needs to be transmitted between the network nodes.

While our approach adds computational tasks at the ABSA, rather than offloading everything for processing at the end nodes, this is reasonable given the ABSA's existing requirement for fast logic to adaptively select measurement bases. Our approach represents a stride toward practical implementation, while also reducing the quantum memory burden at end nodes, thereby fully utilizing the rapid trial rate characteristic of the RGS scheme.

Although the proposed half-RGS possesses a number of desirable characteristics, it remains unclear how it compares with other alternative building blocks. More efficient generation sequences leveraging the local complementation property of graph states could offer advantages such as the inclusion of purification protocols or the extraction of multiple Bell pairs from a single trial [58]. We note that more efficient generation sequences of the RGS via the quantum emitter have recently been proposed [32], [68] during the preparation of this article with different architecture designs and possibly different Pauli frame correction calculations. A detailed analysis of our scheme and a comparison with these alternative methods are deferred to future work.

While studies such as [25], [27], and [28] have investigated the success probability and error analysis of the RGS scheme under conditions of uniform RGSS and ABSA placement, and uniform noise characteristics, the robustness of the RGS scheme under complex noise models and real-world constraints remains unclear. Challenges such as diverse link

characteristics, uneven node placement, and complex traffic models are not amenable to analytic studies and require simulation as can be seen from other link-types [75]. However, existing quantum network simulators [63], [76], [77] do not support the simulation of quantum states comprising hundreds or thousands of entangled qubits. Overcoming this limitation to enable the study of the RGS scheme on quantum network simulators will require innovative approaches. Finally, a detailed analysis of generation time and a performance evaluation comparing mixed RGS and memory-based architectures against RGS-only and memory-only configurations remains a pressing open question.

ACKNOWLEDGMENT

Simulation code that was used to verify our proposed protocols, Pauli frame calculation, and fidelity calculation can be found at https://github.com/Naphann/repeater-graph-state-protocol-based-on-half-RGS/tree/main.

REFERENCES

[1] N. Benchasattabuse, M. Hajdušek, and R. Van Meter, "Architecture and protocols for all-photonic quantum repeaters," in *Proc. IEEE Int. Conf. Quantum Comput. Eng.*, Sep. 2024, pp. 1879–1889, doi: 10.1109/QCE60285.2024.00217.

[2] W. Dür, H.-J. Briegel, J. I. Cirac, and P. Zoller, "Quantum repeaters based on entanglement purification," *Phys. Rev. A*, vol. 59, no. 1, pp. 169–181, Jan. 1999, doi: 10.1103/PhysRevA.59.169.

[3] K. Azuma et al., "Quantum repeaters: From quantum networks to the quantum internet," *Rev. Modern Phys.*, vol. 95, no. 4, Dec. 2023, Art. no. 045006, doi: 10.1103/RevModPhys.95.045006.

[4] H. J. Kimble, "The quantum internet," *Nature*, vol. 453, no. 7198, pp. 1023–1030, Jun. 2008, doi: 10.1038/nature07127.

[5] S. Wehner, D. Elkouss, and R. Hanson, "Quantum internet: A vision for the road ahead," *Science*, vol. 362, no. 6412, Oct. 2018, Art. no. eaam9288, doi: 10.1126/science.aam9288.

[6] W. Kozlowski et al., "Architectural principles for a quantum internet," RFC 9340, Mar. 2023, doi: 10.17487/RFC9340.

[7] M. Hajdušek and R. Van Meter, "Quantum communications," Nov. 2023, *arXiv:2311.02367*, doi: 10.48550/arXiv.2311.02367.

[8] C. H. Bennett and G. Brassard, "Quantum cryptography: Public key distribution and coin tossing," in *Proc. Int. Conf. Comput. Syst. Signal Process.*, 1984, pp. 175–179, doi: 10.1016/j.tcs.2014.05.025.

[9] C. H. Bennett, G. Brassard, C. Crépeau, R. Jozsa, A. Peres, and W. K. Wootters, "Teleporting an unknown quantum state via dual classical and Einstein-Podolsky-Rosen channels," *Phys. Rev. Lett.*, vol. 70, no. 13, pp. 1895–1899, Mar. 1993, doi: 10.1103/PhysRevLett.70.1895.

[10] F. Xu, X. Ma, Q. Zhang, H.-K. Lo, and J.-W. Pan, "Secure quantum key distribution with realistic devices," *Rev. Modern Phys.*, vol. 92, no. 2, May 2020, Art. no. 025002, doi: 10.1103/RevModPhys.92.025002.

[11] A. Broadbent, J. Fitzsimons, and E. Kashefi, "Universal blind quantum computation," in *Proc. 50th Annu. IEEE Symp. Found. Comput. Sci.*, 2009, pp. 517–526, doi: 10.1109/FOCS.2009.36.

[12] J. F. Fitzsimons and E. Kashefi, "Unconditionally verifiable blind quantum computation," *Phys. Rev. A*, vol. 96, Jul. 2017, Art. no. 012303, doi: 10.1103/PhysRevA.96.012303.

[13] R. Cleve and H. Buhrman, "Substituting quantum entanglement for communication," *Phys. Rev. A*, vol. 56, no. 2, pp. 1201–1204, Aug. 1997, doi: 10.1103/PhysRevA.56.1201.

[14] J. I. Cirac, A. K. Ekert, S. F. Huelga, and C. Macchiavello, "Distributed quantum computation over noisy channels," *Phys. Rev. A*, vol. 59, no. 6, pp. 4249–4254, Jun. 1999, doi: 10.1103/PhysRevA.59.4249.

[15] D. Gottesman and I. L. Chuang, "Demonstrating the viability of universal quantum computation using teleportation and single-qubit operations," *Nature*, vol. 402, no. 6760, pp. 390–393, Nov. 1999, doi: 10.1038/46503.

[16] T. J. Proctor, P. A. Knott, and J. A. Dunningham, "Multiparameter estimation in networked quantum sensors," *Phys. Rev. Lett.*, vol. 120, no. 8, Feb. 2018, Art. no. 080501, doi: 10.1103/PhysRevLett.120.080501.

[17] C. L. Degen, F. Reinhard, and P. Cappellaro, "Quantum sensing," *Rev. Modern Phys.*, vol. 89, no. 3, Jul. 2017, Art. no. 035002, doi: 10.1103/RevModPhys.89.035002.

[18] J.-P. Chen et al., "Quantum key distribution over 658 km fiber with distributed vibration sensing," *Phys. Rev. Lett.*, vol. 128, May 2022, Art. no. 180502, doi: 10.1103/PhysRevLett.128.180502.

[19] P. Kómár et al., "A quantum network of clocks," *Nature Phys.*, vol. 10, no. 8, pp. 582–587, Aug. 2014, doi: 10.1038/nphys3000.

[20] W. Ge, K. Jacobs, Z. Eldredge, A. V. Gorshkov, and M. Foss-Feig, "Distributed quantum metrology with linear networks and separable inputs," *Phys. Rev. Lett.*, vol. 121, no. 4, Jul. 2018, Art. no. 043604, doi: 10.1103/PhysRevLett.121.043604.

[21] V. Giovannetti, S. Lloyd, and L. Maccone, "Advances in quantum metrology," *Nature Photon.*, vol. 5, no. 4, pp. 222–229, Apr. 2011, doi: 10.1038/nphoton.2011.35.

[22] D. Gottesman, T. Jennewein, and S. Croke, "Longer-baseline telescopes using quantum repeaters," *Phys. Rev. Lett.*, vol. 109, Aug. 2012, Art. no. 070503, doi: 10.1103/PhysRevLett.109.070503.

[23] L.-M. Duan, M. D. Lukin, J. I. Cirac, and P. Zoller, "Long-distance quantum communication with atomic ensembles and linear optics," *Nature*, vol. 414, no. 6862, pp. 413–418, Nov. 2001, doi: 10.1038/35106500.

[24] N. Sangouard, C. Simon, H. De Riedmatten, and N. Gisin, "Quantum repeaters based on atomic ensembles and linear optics," *Rev. Modern Phys.*, vol. 83, no. 1, pp. 33–80, Mar. 2011, doi: 10.1103/RevModPhys.83.33.

[25] K. Azuma, K. Tamaki, and H.-K. Lo, "All-photonic quantum repeaters," *Nat. Commun.*, vol. 6, no. 1, Apr. 2015, Art. no. 6787, doi: 10.1038/ncomms7787.

[26] S. Muralidharan, L. Li, J. Kim, N. Lütkenhaus, M. D. Lukin, and L. Jiang, "Optimal architectures for long distance quantum communication," *Sci. Rep.*, vol. 6, no. 1, Feb. 2016, Art. no. 20463, doi: 10.1038/srep20463.

[27] P. Hilaire, E. Barnes, and S. E. Economou, "Resource requirements for efficient quantum communication using all-photonic graph states generated from a few matter qubits," *Quantum*, vol. 5, Feb. 2021, Art. no. 397, doi: 10.22331/q-2021-02-15-397.

[28] Y. Zhan, P. Hilaire, E. Barnes, S. E. Economou, and S. Sun, "Performance analysis of quantum repeaters enabled by deterministically generated photonic graph states," *Quantum*, vol. 7, Feb. 2023, Art. no. 924, doi: 10.22331/q-2023-02-16-924.

[29] D. Buterakos, E. Barnes, and S. E. Economou, "Deterministic generation of all-photonic quantum repeaters from solid-state emitters," *Phys. Rev. X*, vol. 7, no. 4, Oct. 2017, Art. no. 041023, doi: 10.1103/PhysRevX.7.041023.

[30] Y. Zhan and S. Sun, "Deterministic generation of loss-tolerant photonic cluster states with a single quantum emitter," *Phys. Rev. Lett.*, vol. 125, no. 22, Nov. 2020, Art. no. 223601, doi: 10.1103/PhysRevLett.125.223601.

[31] B. Li, S. E. Economou, and E. Barnes, "Photonic resource state generation from a minimal number of quantum emitters," *npj Quantum Inf.*, vol. 8, no. 1, pp. 1–7, Feb. 2022, doi: 10.1038/s41534-022-00522-6.

[32] S. Ghanbari, J. Lin, B. MacLellan, L. Robichaud, P. Roztocki, and H.-K. Lo, "Optimization of deterministic photonic-graph-state generation via local operations," *Phys. Rev. A*, vol. 110, no. 5, Nov. 2024, Art. no. 052605, doi: 10.1103/PhysRevA.110.052605.

[33] Y. Hasegawa et al., "Experimental time-reversed adaptive Bell measurement towards all-photonic quantum repeaters," *Nat. Commun.*, vol. 10, no. 1, Jan. 2019, Art. no. 378, doi: 10.1038/s41467-018-08099-5.

[34] Z.-D. Li et al., "Experimental quantum repeater without quantum memory," *Nature Photon.*, vol. 13, no. 9, pp. 644–648, Sep. 2019, doi: 10.1038/s41566-019-0468-5.

[35] K. Tiurev et al., "High-fidelity multi-photon-entangled cluster state with solid-state quantum emitters in photonic nanostructures," Mar. 2021, *arXiv:2007.09295*, doi: 10.48550/arXiv.2007.09295.

[36] Y. Meng et al., "Temporal fusion of entangled resource states from a quantum emitter," *Nature Commun.*, vol. 16, no. 1, Aug. 2025, Art. no. 7602, doi: 10.1038/s41467-025-62130-0.

[37] L. A. Pettersson, A. S. Sørensen, and S. Paesani, "Deterministic generation of concatenated graph codes from quantum emitters," *PRX Quantum*, vol. 6, no. 1, Jan. 2025, Art. no. 010305, doi: 10.1103/PRXQuantum.6.010305.

[38] R. Van Meter and S. J. Devitt, "The path to scalable distributed quantum computing," *Computer*, vol. 49, no. 9, pp. 31–42, Sep. 2016, doi: 10.1109/MC.2016.291.

[39] M. Caleffi, M. Amoretti, D. Ferrari, J. Illiano, A. Manzalini, and A. S. Cacciapuoti, "Distributed quantum computing: A survey," *Comput. Netw.*, vol. 254, Dec. 2024, Art. no. 110672, doi: 10.1016/j.comnet.2024.110672.

[40] D. Barral et al., "Review of distributed quantum computing: From single QPU to high performance quantum computing," *Comput. Sci. Rev.*, vol. 57, Aug. 2025, Art. no. 100747, doi: 10.1016/j.cosrev.2025.100747.

[41] N. Benchasattabuse, M. Hajdušek, and R. Van Meter, "Engineering challenges in all-photonic quantum repeaters," *IEEE Netw.*, vol. 39, no. 1, pp. 132–139, Jan. 2025, doi: 10.1109/MNET.2024.3411802.

[42] H. J. Briegel and R. Raussendorf, "Persistent entanglement in arrays of interacting particles," *Phys. Rev. Lett.*, vol. 86, no. 5, pp. 910–913, Jan. 2001, doi: 10.1103/PhysRevLett.86.910.

[43] M. Hein, W. Dür, J. Eisert, R. Beals, M. Van den Nest, and H. J. Briegel, "Entanglement in graph states and its applications," in *Proc. Int. Sch. Phys. "Enrico Fermi"*, Feb. 2006, vol. 162, pp. 115–218, doi: 10.3254/978-1-61499-018-5-115.

[44] M. Hein, J. Eisert, and H. J. Briegel, "Multiparty entanglement in graph states," *Phys. Rev. A*, vol. 69, no. 6, Jun. 2004, Art. no. 062311, doi: 10.1103/PhysRevA.69.062311.

[45] A. Patil and S. Guha, "Clifford manipulations of stabilizer states: A graphical rule book for Clifford unitaries and measurements on cluster states, and application to photonic quantum computing," Dec. 2023, *arXiv:2312.02377*, doi: 10.48550/arXiv.2312.02377.

[46] D. E. Gottesman, "Stabilizer codes and quantum error correction," Ph.D. dissertation, Dept. of Physics, Mathematics and Astronomy, California Inst. Technol., Pasadena, CA, USA, Jul. 2004, doi: 10.7907/RZR7-DT72.

[47] M. Van den Nest, J. Dehaene, and B. De Moor, "Graphical description of the action of local clifford transformations on graph states," *Phys. Rev. A*, vol. 69, Feb. 2004, Art. no. 022316, doi: 10.1103/PhysRevA.69.022316.

[48] M. Grassl, A. Klappenecker, and M. Rotteler, "Graphs, quadratic forms, and quantum codes," in *Proc. IEEE Int. Symp. Inf. Theory*, 2002, p. 45, doi: 10.1109/ISIT.2002.1023317.

[49] D. Schlingemann, "Stabilizer codes can be realized as graph codes," *Quantum Inf. Comput.*, vol. 2, no. 4, pp. 307–323, Jun. 2002, doi: 10.5555/2011477.2011481.

[50] R. Raussendorf, D. E. Browne, and H. J. Briegel, "Measurement-based quantum computation on cluster states," *Phys. Rev. A*, vol. 68, no. 2, Aug. 2003, Art. no. 022312, doi: 10.1103/PhysRevA.68.022312.

[51] R. Raussendorf and H. J. Briegel, "A one-way quantum computer," *Phys. Rev. Lett.*, vol. 86, no. 22, pp. 5188–5191, May 2001, doi: 10.1103/PhysRevLett.86.5188.

[52] S. J. Devitt, K. Nemoto, and W. J. Munro, "Quantum error correction for beginners," *Rep. Prog. Phys.*, vol. 76, no. 7, Jul. 2013, Art. no. 076001, doi: 10.1088/0034-4885/76/7/076001.

[53] J. Roffe, "Quantum error correction: An introductory guide," *Contemporary Phys.*, vol. 60, no. 3, pp. 226–245, Jul. 2019, doi: 10.1080/00107514.2019.1667078.

[54] M. Varnava, D. E. Browne, and T. Rudolph, "Loss tolerance in one-way quantum computation via counterfactual error correction," *Phys. Rev. Lett.*, vol. 97, no. 12, Sep. 2006, Art. no. 120501, doi: 10.1103/PhysRevLett.97.120501.

[55] R. Van Meter et al., "A quantum internet architecture," in *Proc. IEEE Int. Conf. Quantum Comput. Eng.*, Sep. 2022, pp. 341–352, doi: 10.1109/QCE53715.2022.00055.

[56] A. Russo, E. Barnes, and S. E. Economou, "Photonic graph state generation from quantum dots and color centers for quantum communications," *Phys. Rev. B*, vol. 98, no. 8, Aug. 2018, Art. no. 085303, doi: 10.1103/PhysRevB.98.085303.

[57] I. Tzitrin, "Local equivalence of complete bipartite and repeater graph states," *Phys. Rev. A*, vol. 98, no. 3, Sep. 2018, Art. no. 032305, doi: 10.1103/PhysRevA.98.032305.

[58] B. Li, K. Goodenough, F. Rozpędek, and L. Jiang, "Generalized quantum repeater graph states," *Phys. Rev. Lett.*, vol. 134, no. 19, May 2025, Art. no. 190801, doi: 10.1103/PhysRevLett.134.190801.

[59] C. Jones, D. Kim, M. T. Rakher, P. G. Kwiat, and T. D. Ladd, "Design and analysis of communication protocols for quantum repeater networks," *New J. Phys.*, vol. 18, no. 8, Aug. 2016, Art. no. 083015, doi: 10.1088/1367-2630/18/8/083015.

[60] S. J. Devitt, A. D. Greentree, A. M. Stephens, and R. Van Meter, "High-speed quantum networking by ship," *Sci. Rep.*, vol. 6, no. 1, Nov. 2016, Art. no. 36163, doi: 10.1038/srep36163.

[61] A. Dahlberg et al., "A link layer protocol for quantum networks," in *Proc. ACM Spec. Int. Group Data Commun.*, Aug. 2019, pp. 159–173, doi: 10.1145/3341302.3342070.

[62] R. Van Meter, *Quantum Networking* (Networks and Telecommunications Series). Hoboken, NJ, USA: Wiley, 2014, doi: 10.1002/9781118648919.

[63] R. Satoh et al., "QuISP: A quantum internet simulation package," in *Proc. IEEE Int. Conf. Quantum Comput. Eng.*, Sep. 2022, pp. 353–364, doi: 10.1109/QCE53715.2022.00056.

[64] W. Kozlowski, F. Kuipers, R. Smets, and B. Turkovic, "QuIP: A P4 quantum internet protocol prototyping framework," *IEEE J. Sel. Areas Commun.*, vol. 42, no. 7, pp. 1936–1949, Jul. 2024, doi: 10.1109/JSAC.2024.3380096.

[65] Y. Mori et al., "Scalable timing coordination of Bell state analyzers in quantum networks," in *Proc. IEEE Int. Conf. Quantum Comput. Eng.*, Sep. 2024, pp. 1890–1896, doi: 10.1109/QCE60285.2024.00218.

[66] M. Pant, H. Krovi, D. Englund, and S. Guha, "Rate-distance tradeoff and resource costs for all-optical quantum repeaters," *Phys. Rev. A*, vol. 95, no. 1, Jan. 2017, Art. no. 012304, doi: 10.1103/PhysRevA.95.012304.

[67] H. Shapourian and A. Shabani, "Modular architectures to deterministically generate graph states," *Quantum*, vol. 7, Mar. 2023, Art. no. 935, doi: 10.22331/q-2023-03-02-935.

[68] E. Kaur, A. Patil, and S. Guha, "Resource-efficient loss-aware photonic-graph-state preparation using atomic emitters," *Phys. Rev. A*, vol. 112, no. 6, Dec. 2025, Art. no. 062608, doi: 10.1103/2cbn-448 l.

[69] S. E. Economou, N. Lindner, and T. Rudolph, "Optically generated 2-Dimensional photonic cluster state from coupled quantum dots," *Phys. Rev. Lett.*, vol. 105, no. 9, Aug. 2010, Art. no. 093601, doi: 10.1103/PhysRevLett.105.093601.

[70] A. Russo, E. Barnes, and S. E. Economou, "Generation of arbitrary all-photonic graph states from quantum emitters," *New J. Phys.*, vol. 21, no. 5, May 2019, Art. no. 055002, doi: 10.1088/1367-2630/ab193 d.

[71] C. Gidney, "Stim: A fast stabilizer circuit simulator," *Quantum*, vol. 5, Jul. 2021, Art. no. 497, doi: 10.22331/q-2021-07-06-497.

[72] N. H. Lindner and T. Rudolph, "Proposal for pulsed on-demand sources of photonic cluster state strings," *Phys. Rev. Lett.*, vol. 103, no. 11, Sep. 2009, Art. no. 113602, doi: 10.1103/PhysRevLett.103.113602.

[73] T. Matsuo, C. Durand, and R. Van Meter, "Quantum link bootstrapping using a RuleSet-based communication protocol," *Phys. Rev. A*, vol. 100, no. 5, Nov. 2019, Art. no. 052320, doi: 10.1103/PhysRevA.100.052320.

[74] V. L. Addala, S. Ge, and S. Krastanov, "Faster-than-Clifford simulations of entanglement purification circuits and their full-stack optimization," *npj Quantum Inf.*, vol. 11, no. 1, pp. 1–10, Jan. 2025, doi: 10.1038/s41534-024-00948-0.

[75] K. S. Soon, N. Benchasattabuse, M. Hajdušek, K. Teramoto, S. Nagayama, and R. Van Meter, "Performance of quantum networks using heterogeneous link architectures," in *Proc. IEEE Int. Conf. Quantum Comput. Eng.*, 2024, pp. 1914–1923, doi: 10.1109/QCE60285.2024.00221.

[76] X. Wu et al., "Sequence: A customizable discrete-event simulator of quantum networks," *Quantum Sci. Technol.*, vol. 6, no. 4, 2021, Art. no. 045027, doi: 10.1088/2058-9565/ac22f6.

[77] T. Coopmans et al., "NetSquid, a NETwork simulator for quantum information using discrete events," *Commun. Phys.*, vol. 4, no. 1, 2021, Art. no. 164, doi: 10.1038/s42005-021-00647-8.